Grant Agreement No: 101004761

AIDAinnova

Advancement and Innovation for Detectors at Accelerators

Horizon 2020 Research Infrastructures project AIDAINNOVA

DELIVERABLE REPORT

REPORT ON PROTOTYPES CONSTRUCTION, PERFORMANCE AND ASSESSMENT OF INDUSTRIALISATION

DELIVERABLE: D8.2

Document identifier:	AIDAinnova_D8.2
Due date of deliverable:	End of Month 35 (29/02/ 2024)
Report release date:	22/04/2024
Work package:	WP8: Calorimetry and Particle Identification detectors
Lead beneficiary:	CERN
Document status:	Final

Abstract:

New materials for high precision timing and/or for use in future calorimeters were tested in the various laboratories of project participants, and prototypes were built and tested under high energy particle beams. This report summarises the characterisation of the currently developed novel scintillating materials and the results obtained in testing the detector prototypes to facilitate the selection of the best materials, considering both performance and production capability.

For more information on AIDAinnova, its partners and contributors please see http://aidainnova.web.cern.ch/

The Advancement and Innovation for Detectors at Accelerators (AIDAinnova) project has received funding from the European Union's Horizon 2020 Research and Innovation programme under Grant Agreement no. 101004761. AIDAinnova began in April 2021 and will run for 4 years.

Delivery Slip

	Name	Partner	Date
Authored by	R. Cala ', L. Martinazzoli, E. Auffray V. Babin, P. Bohacek, R. Kucerkova, A. Beitlerova, M. Nikl S. Nargelas, G. Tamulaitis, C. Cecchi, E. Manoni, S. Moneta M. Campajola, G. De Nardo, M. Merola L. Bandiera, M. Moulson I. Sarra, N. Pastrone, S. Brovelli J. Houzvicka., S. Sykorova	CERN IP_ASCR Vilnius INFN Perugia, INFN Napoli INFN Frascati INFN Torino GlasstoPower Crytur	10/01/2024
Edited by	E. Auffray	CERN	14/02/2024
Reviewed by	E. Auffray [Task coordinator] R. Pöschl [WP coordinator] R. Ferrari [WP coordinator	CERN CNRS/IJCLab INFN/Padova	26/02/2024
Approved by	Giovanni Calderini [Deputy Scientific coordinator] Steering Committee		22/04/2024

TABLE OF CONTENTS

Executive summary

This document summarises the characterisation of the new developed scintillating materials and the results obtained with the prototypes on beam test and provides some input for the selection of the best materials, considering both performance and production capability. This document consists of four sections.

After a short introduction, in Section 2 the results of characterisation of various garnet scintillators and work to improve their timing properties are presented, as well as consideration about industrial production of some materials, are presented. In Section 3 results of the performance of various protptypes performed in beam test are summarised. Conclusion is given in Section 4.

1. INTRODUCTION

Activities of AIDAinnova WP8 focus on the development of calorimeters and particle identification detectors for future experiments in high energy physics (HEP). Light-based detectors are the potential technology studied in the Task 8.3. Future detectors in HEP require radiation hard scintillating materials with ultrafast timing response. Several materials were tested in various laboratories participating in the project, exploiting the setups described in Milestone MS32 [1] and detector prototypes were built and tested under high energy particle beams.

In the following sections the description of the scintillation materials studied, their possible production capabilities (Section 2) and the designed and tested prototypes (Section 3) are presented.

Three types of materials were investigated Ultra-Fast lead tungstate (PWO-UF) described in Section 2.1, Garnet materials described in Section 2.2 and nanocomposite scintillators based on lead halide described in Section 2.3. For these three types of material the industrialisation aspect is described in the Sections 2.1.2, 2.2.4, 2.3.4 respectively. In the Section 3, which presents the different detector prototypes, the timing performance for various scintillators with minimum ionising particles and for PWO-UF and PbF2 with electrons is summarised in Sections 3.1 and 3.2.1 respectively. The construction of the electromagnetic calorimeter prototypes with PbF_2 and PWO-UF is presented in Sections 3.2.3 and 3.2.4 and the shaslik prototype with nanocomposite in Section 3.3.2.

2. MATERIALS DEVELOPMENT

Among the various scintillators available, cerium-doped garnet scintillators are considered as potential candidates for radiation detectors in future HEP experiments due to their already demonstrated radiation hardness [2,3,4,5,6]. However, the Ce-activated garnet-type scintillators were considered to be too slow for the future HEP experiments. Therefore, many groups have conducted research and development to study and optimise various garnet materials.

The second research direction was focused on improving the time response of self-activated PWO crystals commonly used in high energy physics [7,8,9]

In the recent years, the development of nanomaterials has led to the emergence of a new class of scintillators: nanocomposite scintillators based on nanomaterial scintillator embedded in a host material. Semiconductor nanocrystals are of great interest due to their high quantum yield and the ease of manufacturing. They have potential application in the development of high-performance scintillators and scintillating components for use in high-energy physics instrumentation. The production of the nanocomposite scintillators containing nanocrystals (NCs) of lead halide perovskites with various compositions were investigated.

The following sections present a summary of the studies performed on these materials and outline the prospects for their large-scale production.

2.1. IMPROVEMENT OF RESPONSE TIME OF SELF-ACTIVATED SCINTILLATOR PWO

2.1.1. Understanding the fast decay process

PWO crystals exhibit a fast luminescence decay [9]. An approach to the further luminescence decay acceleration by heavy doping with lanthanum and yttrium was studied [10,11,12]. The time-resolved photoluminescence (TRPL) spectroscopy and two nonlinear optical techniques with time resolution in subpicosecond domain, the measurement of the transient absorption (TA) in pump and probe configuration and the light-induced transient gratings (LITG) technique, were used (see description in [1]. PWO single crystals were investigated in the temperature range from 10 to 300 K at a wide range excitation intensity.

As evidenced by TRPL spectroscopy and TA measurements, the luminescence of the set of PWO samples under study is strongly dominated by the emission centres of one type: the radiative recombination of excitations at the lattice-building oxyanionic complexes WO_4^{2-} in the regular PWO lattice. The LITG experiments showed that the upper limit of the excitation diffusion length in PWO is 100 nm. Such a low mobility supports the interpretation that the relaxed excitations form self-trapped excitons.

It has been shown that the heavy doping with La and Y results in substantial acceleration of the luminescence decay in PWO, although, at the expense of luminescence efficiency. Such influence of doping on luminescence properties is explained by the distortion of a fraction of the regular WO_4^{2-} complexes by the impurities. The strength of distortion and, consequently, the decay rate depends on the distance between the complexes and impurities.

A nonlinear dependence of the luminescence intensity on the density of self-localised excitons is observed and interpreted by nonradiative Auger-type recombination due to dipole-dipole interaction. This effect accelerates the decay of exciton density, as evidenced by a good fit of the experimental data obtained by transient absorption measurements with the calculation results.

All these results are summarised in [12,13].

The fast heavily doped PWO (PWo Ultra-Fast, PWO_UF) crystals were used in some calorimeter prototypes described in Section 3.2.

2.1.2. Towards production of Ultra-FAST PWO

Crytur has the infrastructure and the technology in place for large scale production PWO_UF crystals. Currently, Crytur is producing PWO_UF on a small scale but can respond swiftly to any increased demand for these crystals. PWO_UF crystals can be grown up to 300mm in length.

2.2. ACCELERATION OF LUMINESCENCE DECAY IN Ce-ACTIVATED AND Mg-CODOPED MULTICOMPONENT GARNETS

The Ce-activated garnet-type scintillators are shown to have high radiation hardness [4,5,6] and are considered as potential candidates for fast detectors in future HEP experiments. However, their luminescence decay time is considered to be too slow for the future applications. Therefore, R&D has been performed in various groups to study the ways to improve the time response of different garnet materials, particularly, by compositional engineering and codoping [14,15,16,17].

In the framework of Task 8.3.1, $Gd_3Ga_xAl_5O_{12}$:Ce,Mg (GAGG:Ce,Mg) and $(Lu,Gd)_3(Ga,Al)_5O_{12}$:Ce,Mg (LuGAGG:Ce,Mg) were fabricated and the impact of codoping on each of these materials has been studied. The first scintillator is currently the most promising candidate in view of the existing knowledge and production maturity (Section 2.2.3) [18]., whereas the second one is still at the level of R&D (Sections 2.2.1, 2.2.2) but is attractive due to the flexibility in its compositional engineering.

2.2.1. Acceleration of luminescence decay by aliovalent codoping in Gd-containing garnet type scintillators

The introduction of Gd in the multicomponent garnets shifts the emitting level of the activator ion Ce^{3+} down in energy and increases the barrier for thermal depopulation of the level. The influence of the Gd sublattice on the excitation transfer in multicomponent garnets was revealed. The excitation transfer via the Gd-sublattice in Ce-activated LuGAGG was studied by time-resolved luminescence spectroscopy at the excitation with 10-keV electrons and the photoexcitation resonantly to the emitting level $5d_1$ of Ce^{3+} to eliminate the stage of excitation transfer through the scintillator matrix (see the schemes in Fig.1). In uncodoped LuGAGG:Ce, the luminescence provoked by the electron beam excitation decays slower than that provoked by the resonant photoexcitation, whereas in Gd-free LuAG:Ce, the decays proceed at the same rate, as shown in Fig. 2. Codoping of LuGAGG:Ce with Mg introduces faster decay component, and the decay kinetics of cathodo- and photo-luminescence coincide.

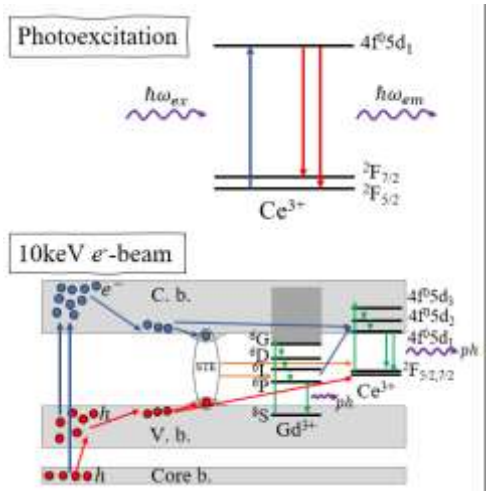

Fig. 1: Schematic presentation of excitation conditions at resonant photoexcitation and in cathodoluminescence experiments in Gd-containing garnets.

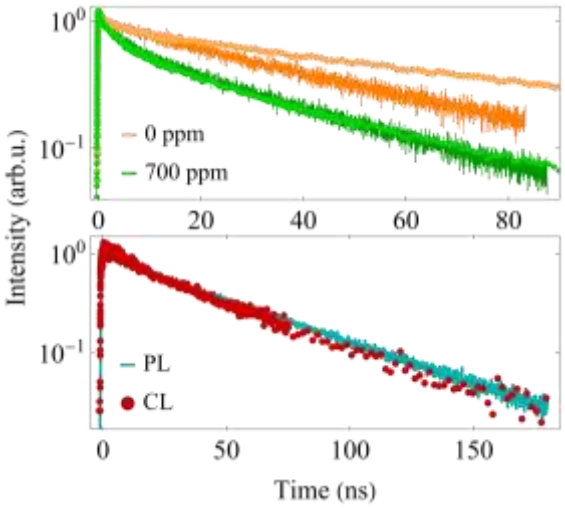

Fig. 2: Normalised room-temperature cathodoluminescence (CL) (dots) and photoluminescence (PL) (lines) kinetics in uncodoped (orange) and heavily Mg-codoped (green) LuGAGG:Ce (upper panel) and in LuAG:Ce containing no Gd (lower panel).

These experimental features were interpreted by the contribution of excitation transfer through the gadolinium subsystem in the scintillator matrix. This assumption was confirmed by the Monte Carlo simulations of the excitation transfer via the Gd-sublattice taken into account. Two terms of Gd^{3+}, ^6P and ^6I, were found to be important in the excitation transfer. We came to the conclusion that the introduction of Gd in the composition of multicomponent garnets results in a delayed transfer of a significant part of excitations to the activator ion and, consequently, deteriorates the decay time of the Ce^{3+}emission. However, the deteriorating influence of gadolinium in the crystal matrix can be eliminated by magnesium codoping. This effect is explained by the overlap of the energy of optical transitions in Gd^{3+} with the absorption band due to the introduction of magnesium. The results are summarised in the paper [19].

2.2.2. Acceleration of luminescence decay in $(Lu,Gd)_3(Ga,Al)_5O_{12}$:Ce,Mg

The influence of magnesium-codoping on luminescence properties of Ce^{3+} ions was also studied in thin films of garnet-type scintillators $(Lu,Gd)_3(Ga,Al)_5O_{12}$:Ce,Mg with Ce content of 1% in all samples under study and different Mg content in the range from 0 to 6000 ppm. The set of samples was studied using time-resolved photoluminescence spectroscopy and transient absorption technique at temperatures ranging from 80 to 600 K.

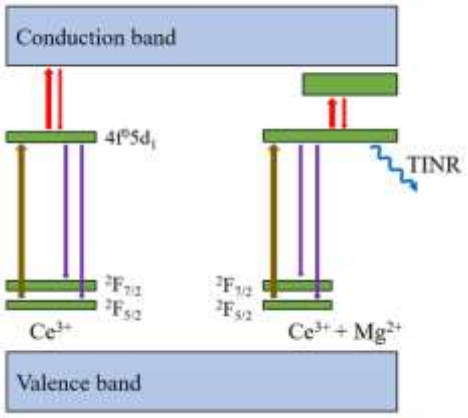

Fig. 3: Schematic presentation of emission centres Ce^{3+} and Ce^{3+}+Mg^{2+} in LuGAGG:Ce,Mg with optical transitions and temperature-independent nonradiative recombination channel indicated.

Two types of emission centres are revealed. The luminescence is dominated by the emission of Ce^{3+} ions, however, the introduction of magnesium results in the formation of modified emission centres Ce^{3+}+Mg^{2+} consisting of Ce^{3+} and Mg^{2+} in close vicinity. The spectrum of the emission at Ce^{3+}+Mg^{2+} centres is similar to that at the regular Ce^{3+}centres up to the Mg content of 6000 ppm. Meanwhile, the magnesium ions introduce a barrier-free channel of nonradiative recombination and a channel for thermal quenching with the activation energy of 200 meV, whereas the barrier for thermal quenching of the regular Ce^{3+} centres equal 480 meV, corresponding to the energy gap between the emitting level $5d_1$ and the bottom of the conduction band. The two types of the emission centres in Mg-codoped crystal are schematically depicted in Fig. 3. It was demonstrated that the properties of magnesium-related emission centres do not depend on the Mg content in the crystal. The increasing Mg content just increases the concentration of Ce^{3+}+Mg^{2+} centres at the expense of the regular Ce^{3+} centres. These results are summarised in [20].

2.2.3. Acceleration of luminescence decay in $Gd_3Ga_xAl_{5-x}O_{12}$:Ce,Mg

Among the various existing garnet materials gadolinium gallium aluminium garnet (GAGG) crystal is currently the most promising candidate for future detectors [18]. The codoping of garnet material with (Ce, Mg) has demonstrated the potential to accelerate the emission [14,15,16,17]. In order to obtain the decay time required for the use of GAGG in the high-luminosity environment of the HL-LHC and future colliders, new GAGG compositions, incorporating with much higher concentrations of Ce and Mg codopants have been developed by the FZU institute (Prague). This led to a substantial reduction in the scintillation decay time, although at the expense of the light yield. CERN, FZU, and Vilnius jointly characterised several new samples demonstrating the light outputs ranging from 500 to 12000 photons/MeV and decay times from 1.7 ns to 25 ns (see Fig. 3). The findings of this study have been summarised Ref. [21]. Despite the reduction in light output, these samples exhibited competitive time resolutions, only 10% worse than those of the current state-of-the-art garnets. Monte Carlo simulations indicate that these new samples meet the performance requirements for the inner region of the future electromagnetic calorimeter of LHCb II (SPACAL).

Based on this study, the optimal composition was defined and research and development aiming at producing larger and more homogeneous samples have started at FZU in collaboration with CRYTUR company (see Section 2.2.4).

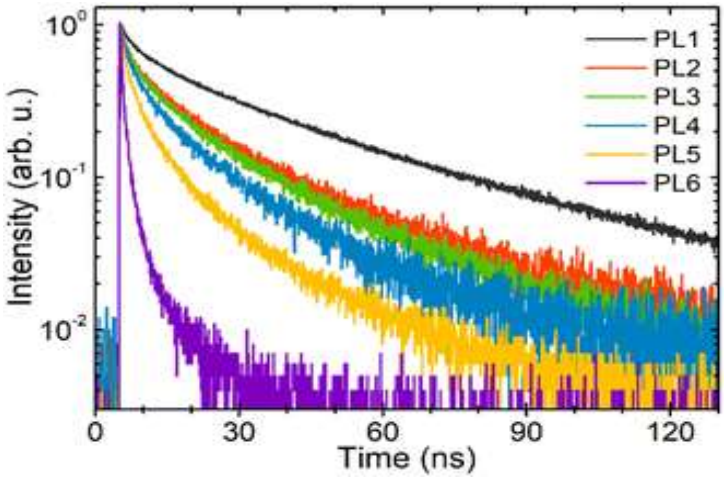

Figure 4: Scintillation decay kinetics for GAGG:Ce,Mg with increasing doping level in samples from PL1 to PL6.

2.2.4. Towards mass production of highly codoped $Gd_3Ga_xAl_{5-x}O_{12}$:Ce,Mg

Among various garnets studied, the most promising one is the standard GAGG due to the existing mass production availability for it. After successfully producing small samples with compositions that meet the decay time requirements for future detectors (see Section 2.2.2), attempts were made to achieve the same composition with micro-pulling down technique by FZU. However, the first attempts did not allow to meet the required decay time.

A joint collaboration between FZU and CRYTUR focused on growing an ingot of GAGG with high compositional homogeneity and heavy Ce doping and Mg codoping by Czochralski method. The first ingot measuring 25 mm in diameter and 48 mm in length (cylindrical part) was successfully grown by CRYTUR. Decay measurements obtained from various parts of the ingot meet the requirements with an effective decay time of 5.0-5.5ns and light yield within 5100-5700 ph/MeV (see Fig. 5). The optical quality of the crystal allows for preparing homogeneous and visually perfect volume elements, see example in Fig. 6.

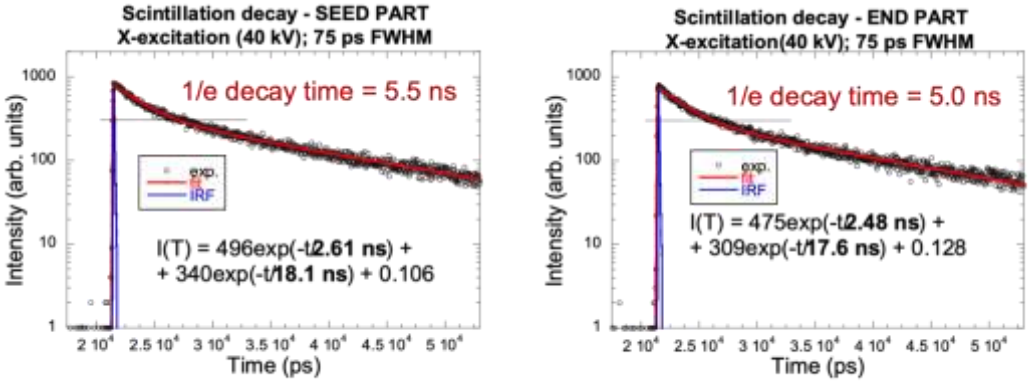

Figure. 5: Scintillation decay spectra for GAGG:Ce, Mg grown by Czochralski in CRYTUR: left decay from seed part, right from end part.

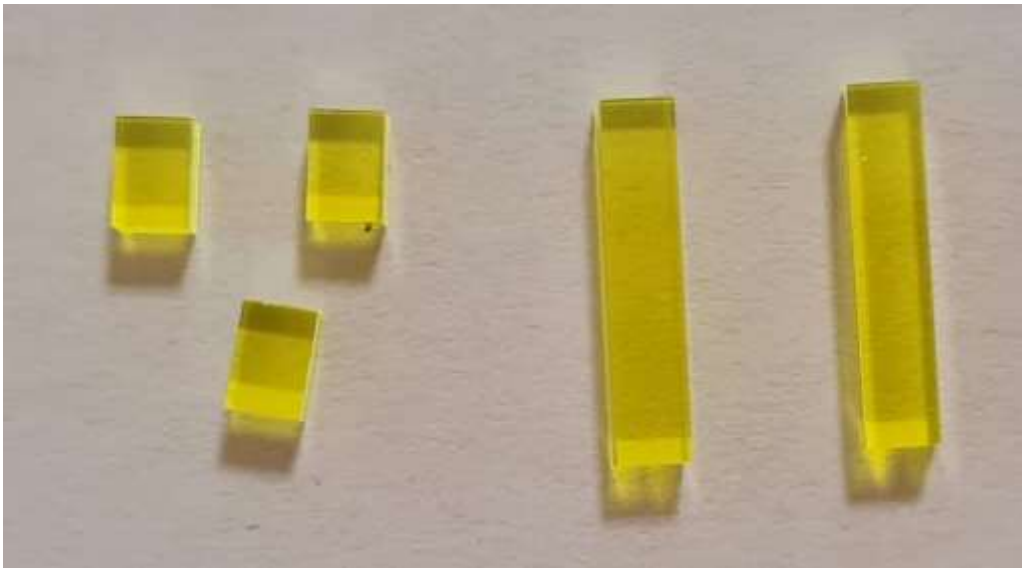

Figure. 6 Volume optical elements prepared from GAGG crystal with characteristics in Fig. 5.

The next steps will focus on precise composition tuning, volume compositional homogeneity and larger crystal dimension and on testing their radiation resistance. Preparation of fibres of $1 \times 1 \times 50$ mm^3 and cubes $10 \times 10 \times 10$ mm^3 for further tests at CERN will follow.

2.3. NANOCOMPOSITE SCINTILLATORS BASED ON LEAD HALIDE PEROVSKITE NANOCRYSTALS

Semiconductor nanocrystals ("quantum dots") are of great interest due to their high quantum yield and ease of manufacture. They have potential applications in the development of high-performance scintillators and scintillating components such as wavelength shifters and scintillating films, for use in high-energy physics instrumentation. Nanocomposite scintillators can be obtained by casting nanocrystals into a transparent polymer matrix, to obtain materials functionally like conventional plastic scintillators. Since inorganic nanocrystals can potentially have O(100 ps) light decay times and O(1 MGy) radiation resistance, nanocomposite scintillators could prove to be ideal for the construction of high-performance detectors that are economical enough to be used for large-volume applications.

Fabrication of nanocomposite scintillators containing lead halide perovskite nanocrystals (NCs) of various compositions, using scalable techniques and plastic matrices made of different polymers using varying polymerisation methods have been investigated by GlasstoPower:

1. $CsPbBr_3$ nanocrystals synthesised in multi-gram scale using ligand-assisted reprecipitation methods in Polymethylmethacrylate/Polylaurylmethacrylate (PMMA/PLMA) nanocomposites via radical mass polymerisation.
2. $CsPbBr_3$ nanocrystals synthesised using ligand-assisted reprecipitation methods and embedded in PMMA or PS (polystyterene) polymeric hosts using solvent evaporation methods.
3. $CsPbCl_3$ nanocrystals using ligands assisted reprecipitation methods in PolyMethylMethacrylate/PolyEthyleneGlycolDimethacrylate PLMA/EGDM nanocomposites via radical mass polymerisation.

2.3.1. $CsPbBr_3$ NCs in PMMA/PLMA

Large-area polyacrylate nanocomposite scintillators based on $CsPbBr_3$ NCs were synthesised using a novel turbo-emulsification approach at room temperature, with minimal waste (see Fig.7). Optical, structural, and radiometric studies confirmed the beneficial interaction between NCs and polyacrylate chains, leading to:

- Strengthening of the scintillator mechanical structure.
- Homogenisation of particles size distribution during polymerisation.
- Passivation of NC defects, resulting in nanocomposite prototypes with luminescence efficiency >90%, and 4800 photons/MeV scintillation yield even at low NC loading.

The nanocomposites also exhibited ultrafast scintillation response time, with over 30% of the radioluminescence decay occurring in the first 80 ps. The radiation hardness of the nanocomposites was verified up to extreme doses of 1 MGy of ^{60}Co γ-rays. The results of this study were published in Ref. [22].

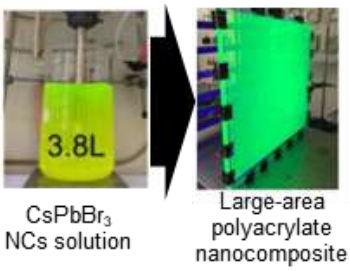

Figure 7: Large area polyacrylate nanocomposite scintillators based on $CsPbBr_3$ NCs.

2.3.2. $CsPbBr_3$ NCs in PMMA/PS

$CsPbBr_3$ NCs were synthetised using a scalable ligand-assisted reprecipitation (LARP) technique and incorporated into polymethylmethacrylate (PMMA) or polystyrene (PS) hosts by solvent evaporation method (see Fig.8). The comparison between PMMA (rich in polar moieties) and PS (lacking acrylic functionalities to passivate surface defects) nanocomposites was conducted using spectroscopic and radiometric techniques. The results revealed the impact of polar carboxylic moieties in polyacrylates on the photophysics and the scintillation properties of $CsPbBr_3$ NCs. Specifically, a dual effect of the polar acrylic groups was found:

i. A fraction of the NC ensemble was damaged in PMMA making them non-emissive.
ii. The remaining NC population experienced a surface curing effect upon polymer encapsulation resulting in the suppression of shallow trapped excitons responsible for delayed emission.

Thermally stimulated luminescence and afterglow experiments were used to explore the impact of polyacrylate moieties on deep trap sites. This extended the knowledge of the scintillation properties of lead halide NCs, even when produced using highly scalable LARP methods. It also clarified the role of polymer embedding in controlling shallow and deep defect states in the NCs. The radiation resistance of plastic nanocomposites was validated up to extremely high γ-ray doses (1 MGy of ^{60}Co γ-rays). These finding were included in a scientific publication currently under review [23].

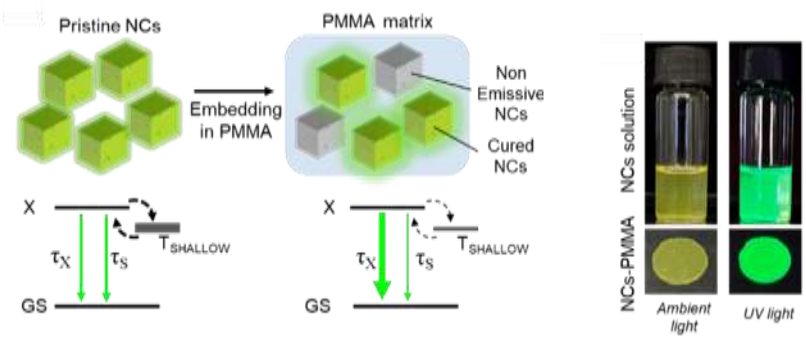

Figure 8: Emission process $CsPbBr_3$ NCs in PMMA.

2.3.3. $CsPbCl_3$ NCs

Highly efficient $CsPbCl_3$ NCs were fabricated for the first time using a high throughput modified LARP technique (see Fig. 9). The resurfacing treatment, responsible for the 30-fold enhancement of optical emission efficiency (now reaching Φ_{PL}=93±6%) was performed directly in the monomeric solution prior to polymerisation, also stabilizing the $CsPbCl_3$ NCs towards the living radical polymerisation of the polyacrylate host. Steady-state and time-resolved radioluminescence experiments reveal a purely excitonic scintillation of the treated particles, with no spurious slow intragap contributions, and ultrafast temporal behaviour due to contributions from multi-excitonic species formed upon interaction with ionizing radiation. Such results filled the knowledge gap in the understanding of nanoscintillators based on lead halide perovskite NCs and provided a potential route to obtain nanocomposite scintillators emitting in the UV spectral range. These finding were included in a scientific publication currently under review [23].

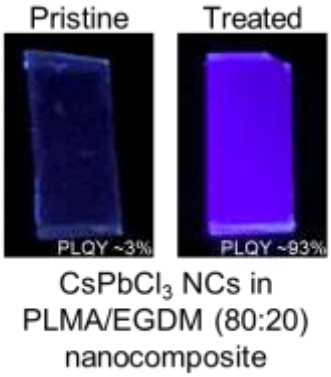

Figure 9: $CsPbCl_3$ NCs embedded in PLMA/EGDM (80:20).

Some of these developed nanocomposite scintillators were used to build innovative shashlik calorimeter, preliminary tests are presented in Section 3.3.

2.3.4. Toward large production of nanocomposite based on $CsPbBr_3$/$CsPbCl_3$

In parallel to the fundamental research activities aimed at the understanding and optimisation of the scintillation of lead halide perovskite (LHP) nanocrystals (NCs) in plastic hosts described in Sections 2.3.1-2.3.3, more scalable approaches to the production of polymeric nanocomposites were investigated. In particular, one bottleneck to the fabrication of heavily doped polymers containing LHP-NCs is the necessity to use photopolymerisation methods that do not damage the optical

properties of the NCs instead of thermal polymerisation routes that are usually employed for mass producing plastic composites. This requirement limits both the maximum NC loading (due to competitive absorption of the UV curing light) and hinders the production of polystyrene composites that cannot be easily photopolymerised. To address this aspect towards large scale production of scintillator nanocomposites based on scintillator polymers, we devise a surface reconstruction process using fluorinated ligands that massively enhance the thermal stability of LHP NCs at the temperatures necessary for the polymerisation of the scintillating polymer polyvinyl toluene (PVT) and adapted its manufacture to reduce the thermal budget.

By using this approach, we were able to produce composites containing as much as 10% of $CsPbBr_3$ NCs while preserving the optical properties of the NCs in solution (see Fig. 10).

This protocol is now included in a manuscript that will be submitted for publication soon.

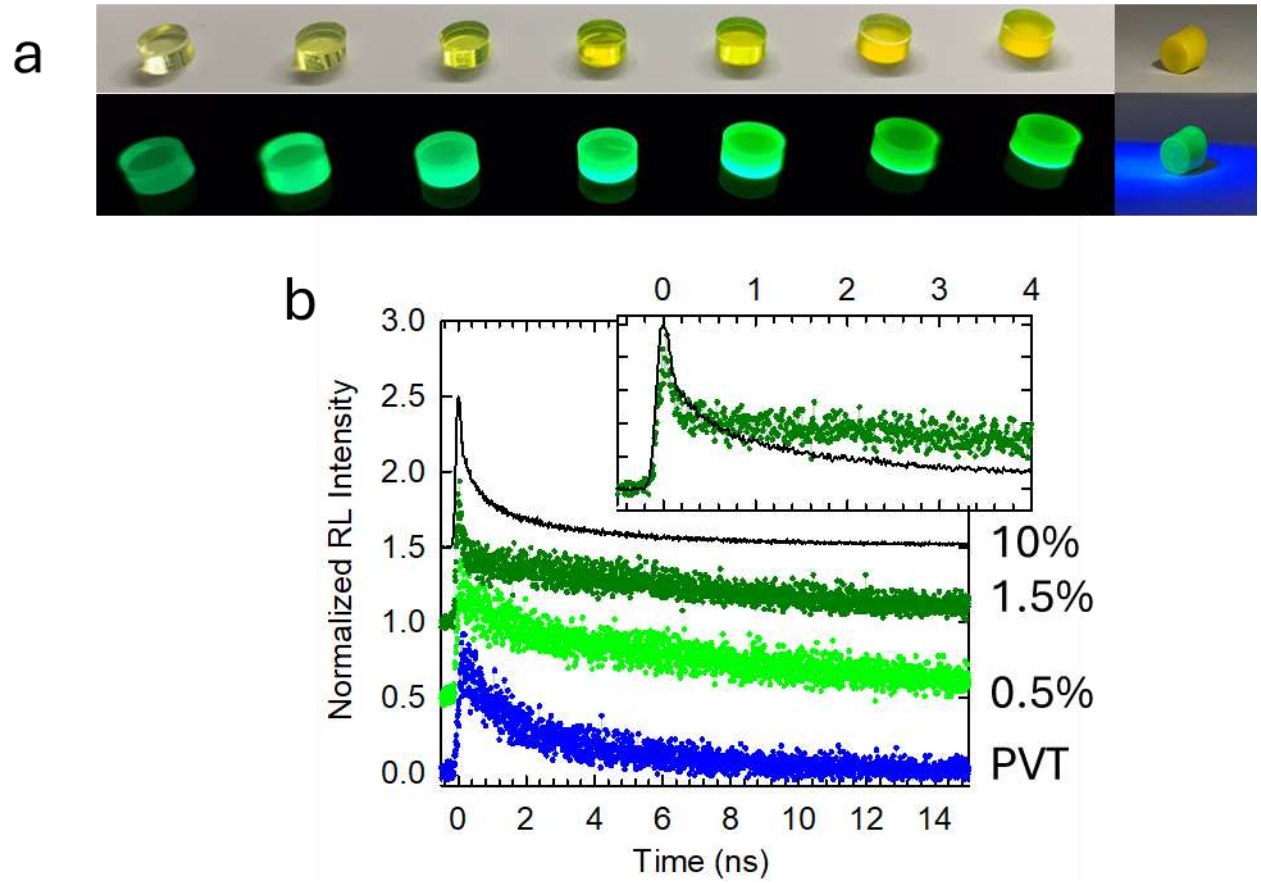

Figure 10: a) PVT nanocomposites containing fluorinated $CsPbBr_3$ NCs (concentration 0.01-10% left to right). b) Scintillation decay of pure PVT (blue), and PVT nanocomposites containing increasing amounts of CsPbBr3 NCs, showing increasing prompt emission with increasing Nc loading.

On the chemistry front, we further consolidated the synthesis of LHP NCs with large scale methods at room temperature in order to produce single batches of various grams.

3. MAIN RESULTS ON PROTOTYPES

The activities in WP8 aim to develop cutting edge calorimeters and particle ID detectors. Task 8.3.1 focuses on developing detectors based on scintillating materials for both future calorimeters and timing detectors. The performance of known scintillators and newly developed materials such as

GAGG, PWO ultra-fast (PWO-UF) and nanomaterials (see Chapter 2) have been assessed using high-energy particles beams both at CERN and Frascati. The results of these studies are summarised in the following sections.

3.1. TIMING PERFORMANCE OF SCINTILLATORS PIXELS WITH MINIMUM IONISING PARTICLES

Proper reconstruction of events is expected to pose a significant challenge in upcoming high-energy physics experiments, primarily due to the high track density and resultant event pile-up. To enhance energy measurements, a precise assessment of time information at both the calorimeter and vertex levels holds the potential to alleviate pile-up effects. An estimated time resolution of approximately 20 ps (σ) has been identified as necessary for such applications [24] and the ability to approach this limit has already been demonstrated using fast inorganic scintillators with high light yields, such as LYSO:Ce, LSO:Ce,Ca, and aluminium garnet crystals [25, 26], coupled with silicon photomultiplier devices.

In recent years, extensive research and development efforts have been underway in various groups to explore new materials and processes. For such a reason, two test beam campaigns were conducted at the H2 beamline at CERN SPS in September 2022 and June 2023 by the CERN group with the test bench setups described in [1]. The goal was to evaluate the timing performance under high-energy pion exposition of (mainly) $2 \times 2 \times 10$ mm^3 pixels made from various scintillating materials coupled to SiPMs and whose signals were readout using custom high-frequency electronics [27,28] (a picture of the setup is shown in Fig. 11). The materials under investigation included standard scintillators such as LYSO:Ce, LSO:Ce,Ca, GAGG:Ce, GAGG:Ce,Mg (from different manufacturers). Furthermore, crystals primarily utilising Cherenkov radiation for timing applications, such as $PbWO_4$, PbF_2, BGO, BSO and BGSO, and cross-luminescent scintillators, e.g. BaF_2 and BaF_2:Y, were also tested. The best result of about $\sigma = 12$ ps was achieved for a $2 \times 2 \times 10$ mm^3 LSO:Ce:Ca sample. Notably, among the tested samples, GFAG, GAGG:Ce,Mg, BaF_2 and BaF_2:Y exhibited excellent timing performances, achieving a single-detector time resolution of approximately $\sigma = 14$ ps. This result is comparable to LYSO:Ce, the leading material for CMS barrel timing layer for the LHC Phase 2 [29].

To predict the anticipated performance of these materials, a GEANT4-based simulation framework was constructed and employed. The obtained simulation results were then compared to the measured ones, presented in Figure 12. Currently, a paper summarising the outcomes from both test beams is in preparation.

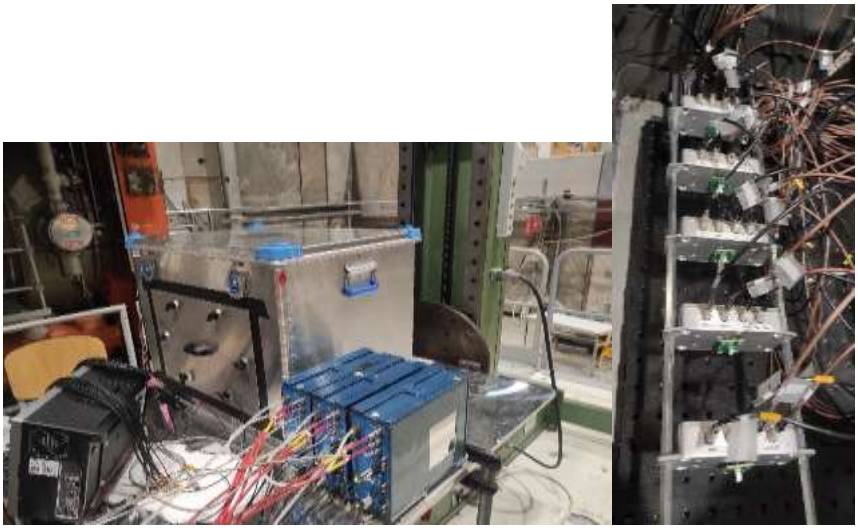

Figure 11: Photos taken during the 2023 test beam campaign. The image on the left features the dark-tight box containing the samples with three DWCs in front. On the right, the picture depicts the samples connected to their respective readout boards, shielded by a metal case.

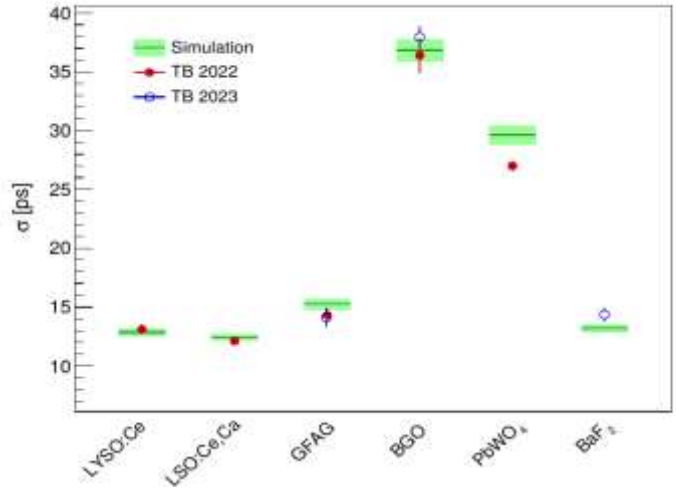

Figure 12: Comparison of single-detector time resolutions under mips exposure for various materials, derived from test beam measurements conducted in both the 2022 and 2023 campaigns, and their corresponding simulation results. Error bands, representing one standard deviation, are included for the simulated output values.

3.2. ELECTROMAGNETIC CALORIMETER PROTOTYPES

The INFN groups at Frascati and Torino, with significant participation of from collaborators from INFN Ferrara and the University of Insubria (Como), are developing ultra-fast, highly compact electromagnetic calorimeter prototypes based on dense, high-*Z* crystals providing very fast light output with superior rate and radiation resistance for use in experiments at next-generation colliders such as the ILC, FCC-*ee*, and, especially, the muon collider. In the near term, the technology developed could be applied in experiments at the HL-LHC, as well as to intensity-frontier experiments such as HIKE, proposed to measure ultra-rare kaon decays at the CERN SPS.

In many high-rate applications, the calorimeter must provide as much information as possible about the shower topology. The Frascati-Torino prototypes are based on the CRILIN design [30], which

features longitudinal segmentation to provide muon identification in high-intensity collider experiments or photon/neutron discrimination in the case of HIKE. Very few studies have been performed to date with longitudinally segmented crystal calorimeters. Readout with SiPMs would greatly facilitate the design of a compact, longitudinally segmented calorimeter. This will require the use of SiPMs with excellent radiation resistance and timing performance, as well as carefully optimised front-end electronics.

A natural candidate for a fast, dense crystal is lead fluoride (PbF_2), a Cherenkov radiator that provides very fast signals. The small-angle calorimeter for the PADME experiment used an array of 25 lead crystals of 30 × 30 × 140 mm^3 and obtained a time resolution of 81 ps and double-pulse separation of 1.8 ns for 100–400 MeV electrons [31]. However, at high radiation doses, loss of transparency to Cherenkov light could be significant for PbF_2, as suggested by existing studies with ionising doses of up to O(10 kGy) [32,33,34]. For applications involving higher doses (> 10 kGy), a good, radiation-hard alternative could be optimised lead tungstate ($PbWO_4$, PWO) [8,11,12,13,35]. In particular, ultrafast PWO (PWO-UF) with a decay time constant of 640 ps, good light yield, and high radiation tolerance has recently been developed (see Section 2.2.1) [11,12].

The coherent interactions of high-energy electromagnetic (EM) particles in high-Z crystals are known to enhance the cross sections for EM shower processes, leading to excellent prospects for the construction of very compact calorimeters with aligned crystals providing small effective values of the radiation length. This effect has never been exploited in calorimetry and could lead to a new paradigm for high-resolution calorimetry at high energies. Determination of the crystallographic axes for large numbers of crystals with cm-scale dimensions will require the development of new measurement techniques, and alignment of the crystals will present novel engineering challenges, leading to significant advances in crystallography and crystal processing.

3.2.1. Timing resolution with single PbF_2 and PWO-UF crystals

Test beam measurements of individual PbF_2 and PWO-UF crystals were performed in summer 2021 at the Frascati BTF and the SPS North Area, followed by additional tests in fall 2022 in which some of the first commercially available samples of PWO-UF (Crytur, Turnov, Czech Republic) were also tested. These measurements, which were carried out with the test bench setups described in [1], were focused on understanding the best possible time resolution that can be obtained, studying the systematics of light collection in the small crystals, and validating the CRILIN choices of SiPMs and the design of the readout electronics. In autumn 2022, single 10 × 10 × 40 mm^3 crystals of PbF_2 ($4.3X_0$) and PWO-UF ($4.5X_0$) were exposed to high-energy (60–120GeV) electron beams at the SPS H2 beamline. Each crystal was viewed by a matrix of four Hamamatsu 14160-4010 SiPMs (4 × 4 mm^2, 10 μm pixel size), which were read out in pairs, providing independent readout channels for the left and right sides of the crystal (Fig. 13).

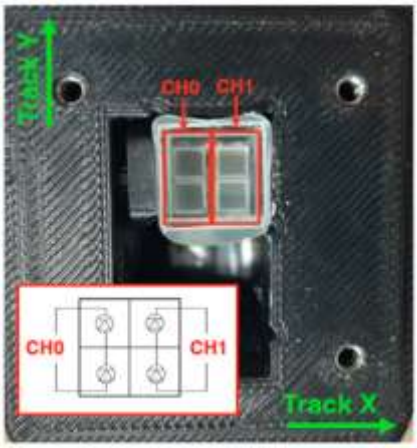

Figure 13: Single crystal read out with 2 × 2 matrix of four 4 × 4 mm^2 SiPMs. The SiPM series wiring scheme providing two readout channels is shown in the inset.

The SiPM was chosen to represent a plausible choice in the current state of the art for high-speed response, short pulse width, and good radiation resistance. The signals from the SiPMs were amplified with the CRILIN electronics and digitised at 5 GS/s. Analysis of the test beam data was recently completed and submitted for publication [36]. Fig. 14 shows the time resolution obtained for single crystals as a function of deposited energy, in the "front" (SiPMs on downstream end of crystals, viewing upstream) and "back" (SiPMs on upstream end of crystals, viewing downstream) configurations. The time resolution was obtained from the differences Δt between the times measured from each of the readout channels. For both crystal types, the time resolution is significantly better in the "back" configuration: due to the highly directional nature of the Cherenkov light, the light arriving at the downstream end of the crystal is highly localised, giving rise to a dependence of the light arrival time on the position of particle incidence that is thoroughly randomised when the light is reflected upstream. Due to the scintillation component, the light yield for PWO-UF (~0.6 p.e./MeV) is approximately twice that for PbF_2 (~0.3 p.e./MeV), but due to the purely Cherenkov emission for PbF_2, its time resolution is slightly better. The time resolution obtainable from the combination of either crystal, PbF_2 or PWO-UF, with the chosen SiPM and CRILIN electronics is excellent: about 12 ps for PbF_2 and 19 ps for PWO-UF in "back" configuration for an energy deposit of 5 GeV (corresponding to the threshold to be used in HIKE).

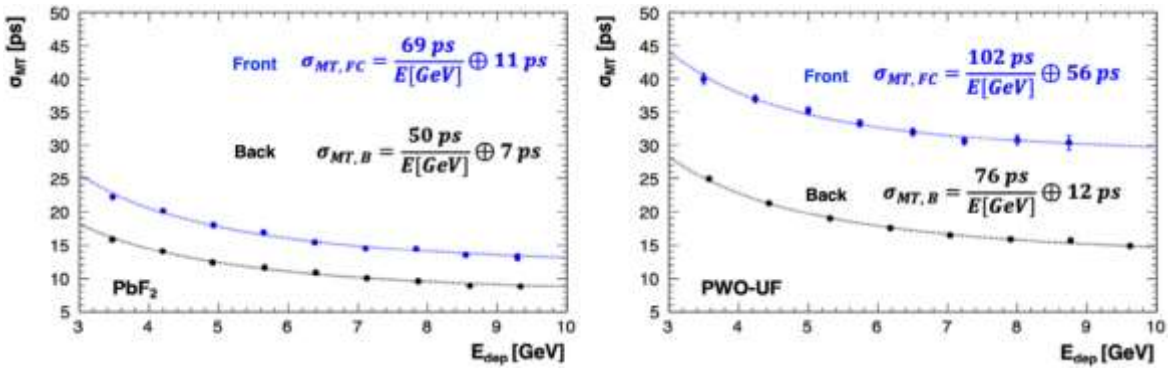

Figure 14: Time resolution obtained with single 10 × 10 × 40 mm^2 crystals of PbF_2 (left) and PWO-UF (right) as a function of deposited energy, from beam tests with high energy electrons. The blue (black) curves are for data taken in "front" ("back") configurations.

3.2.2. Radiation resistance of PbF_2 and PWO crystals

In collaboration with the authors of [32], we performed transmission measurements with a 40-mm path length on PbF_2 and PWO-UF crystals exposed to gamma rays from a ^{60}Co source at the ENEA Calliope facility. After irradiation to 361 kGy, the PbF_2 sample (SICCAS, Shanghai, China) demonstrated a ~ 20% loss of transmission at 400 nm, with the onset of transparency at 320 nm, up from 250 nm before irradiation, as shown in Fig. 15, left. Substantial recovery of the transmission of the PbF_2 crystals was observed after several days of annealing in natural light. By contrast, even after irradiation to 2106 kGy, the PWO-UF sample showed no increase in the wavelength of onset of transparency (350 nm) and a loss of transparency of only about 5% at longer wavelengths, as shown in Fig. 15, right.

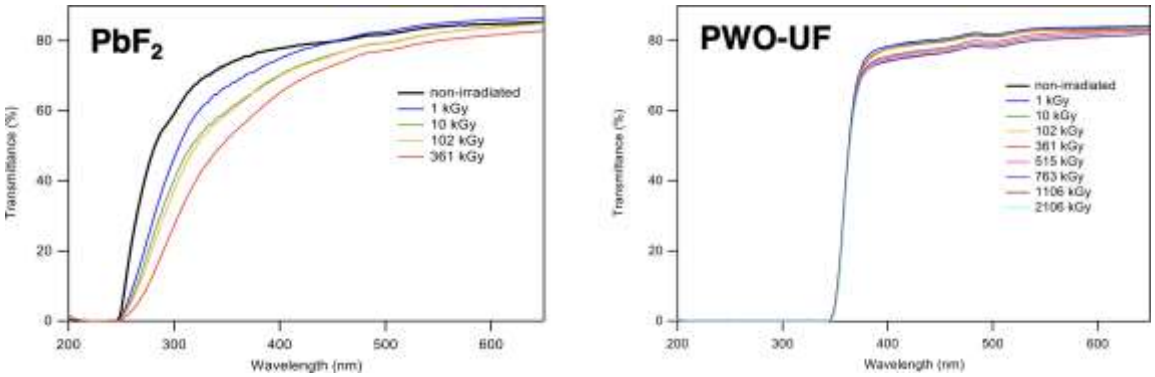

Figure 15: Transmission spectra for PbF_2 (left) and PWO-UF crystals (right), after irradiation at various doses with γ-rays from ^{60}Co.

3.2.3. Development of a prototype for a fast, high-granularity crystal calorimeter with longitudinal segmentation

After a short test in the CERN PS T9 area in June 2023, a two-layer, 3 × 3 crystal CRILIN prototype was tested extensively with 450 MeV electrons at the Frascati BTF in June 2023 and with 20-120 GeV electrons and 40 GeV mips at the SPS H2 beamline in August 2023 to validate the segmentation scheme, measure the time resolution with reconstructed clusters, study the effects of design optimisations such as the choice of crystal surface treatments and wrapping materials, and evaluate the performance of the engineering solutions adopted.

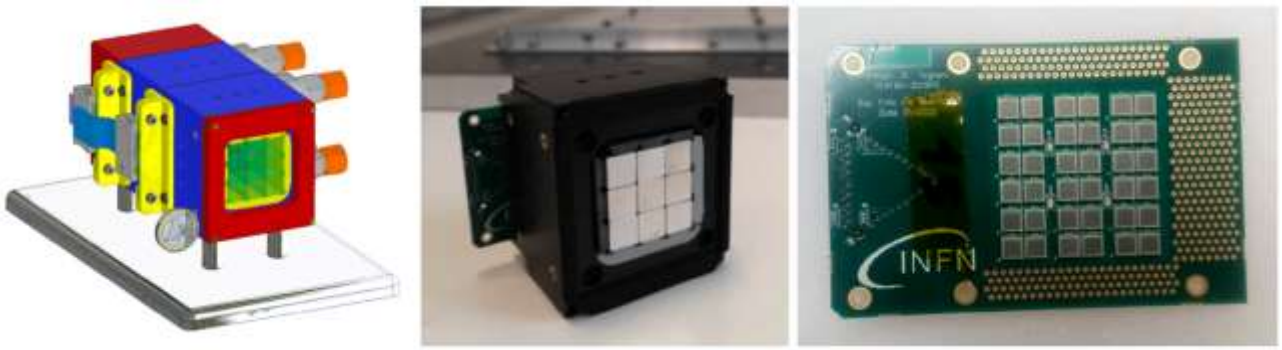

Figure 16: Two-layer 3 × 3 crystal CRILIN prototype: mechanical drawing (left), assembled front module (centre), and PCB with SiPMs for one layer (right).

The 18-crystal prototype is shown in Fig. 16. The light is read out in the same manner as for the single crystals tested in 2021–2022 (see Section 3.2.1), with two channels per crystal, for a total of 36 channels. Modular electronics for power distribution, SiPM signal processing, and control have also been developed and were validated during these beam tests.

Although the data collected during the July and August test beams are still under analysis, some preliminary findings are already apparent. Among the various techniques for crystal surface preparation and wrapping, the best time resolution was obtained with ground crystal surfaces and Teflon wrapping as a diffuse reflector. With this wrapping scheme, the single-crystal time resolution for PbF_2 as measured from Δt was seen to improve from 12 ps to 9 ps. A first attempt to estimate the time resolution for cluster reconstruction was limited by two aspects of the readout system. The time resolution as measured from Δt between layers has been estimated preliminarily to be about 40 ps, dominated by the synchronisation jitter between DRS4 chips in the CAEN V1742 digitiser boards used. The absolute time resolution measured with respect to a fast scintillator used as a time reference receives an additional contribution from the reference detector. Work is in progress to minimise both contributions. The distributions of the energy deposited in each crystal and in the entire assembly were measured and compared to results from the simulation described in [36], with excellent agreement, which was made easier using SiPMs from the same production lot with good gain uniformity.

3.2.4. Development of prototypes for a calorimeter with oriented crystals

The potential gains from aligning the crystals, as well as the procedures and mechanics needed, are under study. In summer 2021, in a joint test with the CRILIN and STORM collaborations in H2, a tagged photon beam was used to measure the enhancement of shower processes in thicker PbF_2 and PWO crystals as a function of angular alignment, correlating variables such as the energy dispersed in the crystal and multiplicity of charged particles produced in the shower with the production of Cherenkov and scintillation light in the crystals. STORM collected similar data with electron beams in summer 2021 and 2022. The data are still under analysis but, as a preliminary generalisation, the effective radiation length for crystals of 2–4 cm thickness is reduced by ~30% by beam alignment with the crystal axis (specifically, the <100> axis for PWO and the <110> axis for PbF2), with an angular acceptance of about 1 mrad [37].

The OREO collaboration, which is continuing the work of STORM, is constructing a PWO-UF calorimeter prototype in which the axes of the crystals on the front layer are aligned (Fig. 17).

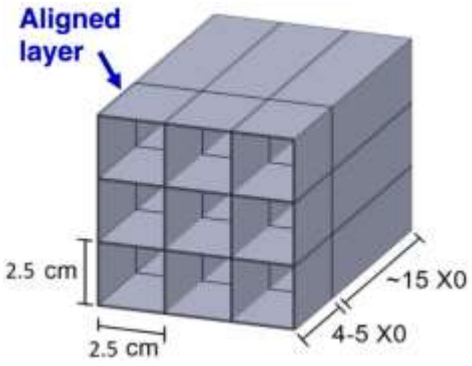

Figure 17: Schematic diagram of the OREO prototype to demonstrate the concept for a calorimeter with aligned crystals. The <100> axes of the crystals in the front layer (depth 4.5 X0) are mutually aligned to within ~0.2 mrad, allowing the prototype to be aligned with the direction of beam incidence

In addition to allowing studies of the variation of the energy deposition, radiation length and Molière radius with beam energy and crystal alignment, the OREO prototype will serve as a platform for developing the procedures and mechanics needed to build a calorimeter with aligned crystals. Much progress has been made over the past year in the areas of measuring the crystallographic quality (mosaicity, axis uniformity, and absence of internal stresses) and determining the axis orientation of PWO-UF crystals both via high-resolution X-ray diffraction and photoelastic analysis with laser conoscopy, as well as in defining a proof-of-concept calorimeter geometry with a Geant4 model including the shower development in oriented crystals, and above all, developing the techniques and equipment needed for the alignment of a matrix of scintillator crystals [38]. The alignment system is based on motorised optomechanical components and features laser interferometric control of the crystal orientation during the entire procedure; it was used to create two matrices of 25 × 25 × 40 mm^3 crystals, whose axes were then measured with electron beams in beam tests in summer 2023. The first prototype, a 1 x 3 crystal matrix, was tested in the PS T9 area in July; the second, a 2 x 2 matrix, requiring the alignment of stacked layers, was tested in the SPS H2 area in August. The prototypes are shown in Fig. 18. Preliminary results show simultaneous and correlated variations in the scintillation yield for all crystals when the prototypes are rotated, suggesting that alignment between the crystallographic axes of the crystals in each prototype to the level of 0.2 mrad has been achieved.

Figure 18: 2 x 2 and 1 x 3 assemblies of crystals with pre-alignment of crystallographic axes during the summer 2023 beam tests. A silicon mirror used to provide an absolute angular reference for the whole assembly is visible at the upper left in each case.

3.3. NANOCAL: AN INNOVATIVE SHASHLIK CALORIMETER WITH NANOCOMPOSITE SCINTILLATORS

The goal of the NanoCal project is to evaluate the potential for the use of nanocomposite scintillators (see Section 2.3) in calorimetry. To this end, fine-sampling shashlik calorimeter prototypes are being constructed with both conventional and NC scintillators and tested side-by-side with electron and minimum-ionising particle beams, allowing the performance gains obtained from the use of NC scintillators to be directly measured. NanoCal is an AIDAinnova WP 13.5 blue-sky project but is directly related to the work on nanocomposite scintillating materials and their industrialisation carried out in WP 8.3.1 (see Section 2.3).

3.3.1. Development of nanocomposite scintillators for NanoCal project

In view of the encouraging results obtained with $CsPbBr_3$ nanocrystals in PMMA reported in [20, 22, 34] (see also Section 2.3), the nanocomposite used for the first NanoCal prototypes (constructed as discussed in the following section) consisted of 0.2% (w/w) $CsPbBr_3$ nanocrystals in a UV-cured PMMA matrix (Fig. 19). These nanocrystals absorb strongly in the near-UV to blue regions and have an emission peak in the green at 520 nm.

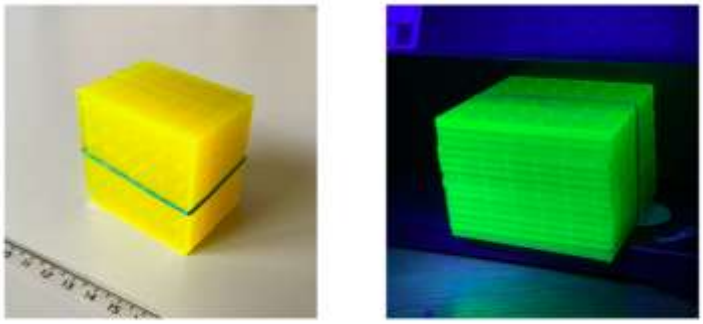

Figure 19: Shashlik tiles made of $CsPbBr_3$ nanocomposite scintillator, in ambient light (left) and under ultraviolet light (right).

As discussed below, tests with mips in the CERN H2 beamline and with cosmic rays showed a disappointing light yield from these prototypes, and laboratory tests with radioactive sources and cosmic rays demonstrated that the light yield from the scintillator was lower than expected. Two possible causes were identified:

1. Excessive self-absorption of the light emitted by the nanocrystals.
2. Inefficient transfer of energy deposited in the plastic matrix to the nanocrystals and/or insufficient concentration of nanocrystals for efficient stimulation by ionisation energy losses from single particles.

The issue of self-absorption can be addressed by the addition to the composite of dyes with large Stokes shift, as in a conventional scintillator. However, because the $CsPbBr_3$ nanocrystals emit at 520 nm, it is difficult to implement two stages of wavelength shifting (one each in the scintillator and in the readout fibres) while still maintaining good photodetector response. A possible solution is illustrated in Fig. 20: the spectral response of the $CsPbBr_3$ nanocrystals is shifted to the blue by the substitution of about half of the bromine atoms with chlorine after production. Then, a WLS compound, coumarin-6, is added to the solution to provide a large Stokes shift, which also restores the emission of the nanocomposite at about 520 nm. A prototype based on this principle was tested, as discussed below.

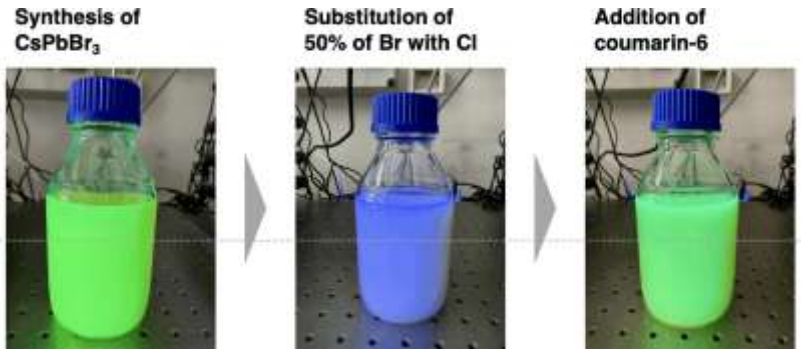

Figure 20: Preparation of monomer solution for nanocomposite with caesium lead halide perovskite with coumarin-6 WLS.

Regarding the second point, PMMA does not have the aromatic structure of polystyrene (PS) or polyvinyltoluene (PVT) and so does not have the level structure for excitation by ionising radiation and de-excitation via Foerster transfer to the nanocrystals, as occurs between the aromatic rings and primary fluors for a conventional scintillator. Fluorescence in PMMA-based nanocomposites is expected to occur primarily from the directly stimulation of the nanocrystals by the incident radiation. The simplicity of this mechanism, combined with the good optical and physical properties of PMMA gives rise to the fast deexcitation times and robust nature of PMMA-based nanocomposites. However, the concentration of the nanocrystals may be insufficient for direct stimulation. Because $CsPbBr_3$ nanocrystals have poor thermal stability, it is convenient to produce the nanocomposites by UV polymerisation, but the absorption of UV light by the nanocrystals limits their concentration to a fraction of a percent.

The poor thermal stability of $CsPbBr_3$ nanocrystals is the result of degradation or detachment of the ligands at the surface of the nanocrystals at the temperatures required for thermal polymerisation. One solution to this problem is to use surface ligand engineering techniques to passivate the surfaces of the nanocrystals with metal ions [40]. The nanocrystals with improved stability can then be used to make thermally polymerised composites, allowing not only PMMA, but also aromatic plastics such as PS or PVT, to be used for the matrix, opening the possibility of efficient Foerster energy transfer from the matrix to the nanocrystals.

To test these ideas, small samples of various scintillators were produced and exposed to 1-5 GeV electron and mip beams in the CERN PS T9 beamline in October 2023 and to 450 MeV electrons at the Frascati BTF in November 2023, as well as to cosmic rays. The scintillator samples, shown in Fig. 21, include two nanocomposites, labelled “Bic 4” and “Bic 5”, made with $CsPbBr_3$ nanocrystals passivated with ytterbium ions and thermally polymerised in PVT at a concentration of 1%. Both samples contain 1.5% PTP to assist with the energy transfer to the nanocomposites; the sample labelled “Bic 5” additionally contains a small amount of the perylene dye described in [39], which shifts the emission to orange. The Figure 21 also shows various samples of custom-produced conventional organic scintillators: “Protvino”, a PVT scintillator with 1.5% PTP and 0.04% POPOP as fluors (as in [41]), “Bic 1”, a blue scintillator using a benzothiophene dye, and “Bic 2” and “Bic 3”, two green scintillators based on coumarin-6, the dye used to shift the emission from $CsPb(Br,Cl)_3$ from blue to green in Fig. 21. While the data are still under analysis, preliminary results indicate that the nanocomposite scintillators have a light yield of about 60% of that of the “Protvino” control sample (with 10-20% spectral corrections). An additional result is that “Bic 3”, which contains 0.04% coumarin-6 and 0.04% of the benzothiophene dye, as well as 1.5% PTP, gives 160% of the light

output of the Protvino scintillator, making this sample an interesting candidate for study as a high-yield conventional green scintillator in its own right.

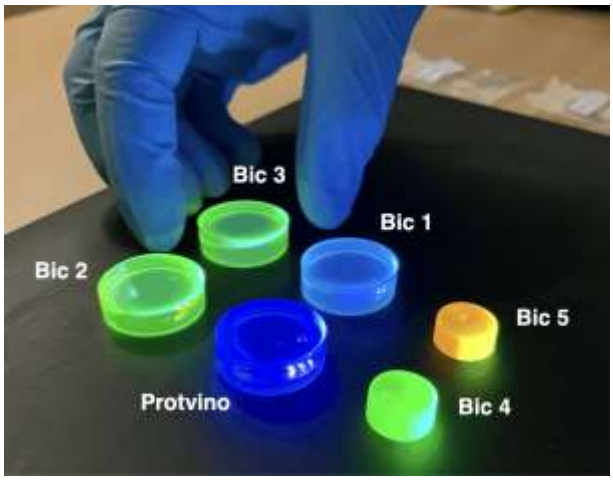

Figure 21: Conventional organic and nanocomposite scintillator samples tested in fall 2023 at CERN and Frascati

The surfaces of the nanocrystals can also be passivated with a halide-rich surface layer. A series of nanocomposite scintillator samples made with fluorine passivated $CsPbBr_3$ nanocrystals at various concentrations in PVT, with and without additional dyes, were made in preparation for a series of measurements with 450 MeV electron beams at the Frascati BTF in Spring 2024 (Fig. 22). These measurements, together with those carried out in fall 2023, will allow a systematic optimisation of the choice of nanoparticle and any additional fluors. Once a suitable nanocomposite scintillator has been identified, it will be possible to construct a test module such as those previously tested with the PMMA-based nanocomposites, as further described in the next section.

Figure 22: Samples of $CsPbBr_3$ nanocomposites at concentrations of 1.0-2.5% with and without PTP and/or perylene dyes, together with control samples containing no nanocrystals Light yields for these samples will be measured at the Frascati BTF in February 2024.

3.3.2. Construction of shashlik calorimeter prototypes with innovative scintillators

To establish a baseline for the understanding of the issues involved in constructing calorimeter modules with NC scintillator, various small test assemblies were constructed. These consist of a short, fine sampling shashlik stack of about 5 cm in thickness (about $1.5X_0$) based on the design for the PANDA forward spectrometer electromagnetic calorimeter [42], which was originally developed for the KOPIO experiment [41]. The thicknesses of the scintillator tiles and lead absorber foils are 1.5 mm and 0.275 mm, respectively, for a sampling fraction of about 39%. The tiles are 55 x 55 mm^2 in cross section and feature 36 1.3-mm holes for the shashlik fibres. The first module to be constructed was a control module made with tiles of conventional extruded polystyrene scintillator from the PANDA prototypes, with 1.5% PTP and 0.04% POPOP as fluors. This scintillator has an emission peak at 425 nm; Kuraray Y-11(200) blue-to-green wavelength shifting fibres (WLS) were used for light readout.

The nanocomposite scintillators for the test modules were obtained by UV polymerisation between glass plates of the solution of $CsPbBr_3$ nanocrystals in the MMA monomer (Fig. 23, left). The shashlik tiles (see Fig. 19) were then laser cut from the resulting sheet of material. To read out the 520-nm green light from the nanocrystals, a custom production was commissioned to Kuraray of a 1-mm single clad WLS fibre dyed with the perylene dyad described in [39] at a concentration of 200 ppm; this fibre is referred to as NCA-1(200). An additional module was constructed with Kuraray's existing O-2(100) green-to-orange WLS fibre as a point of comparison. The light from the fibres was read out with a Hamamatsu 13360-6050 SiPMs (6×6 mm^2, 50 μm pixel size) and a fast amplifier with a gain of 4. The fibres were bundled into a ferrule for coupling to the SiPM with optical grease. The shashlik stacks for a few of these modules are shown in Fig. 23 right.

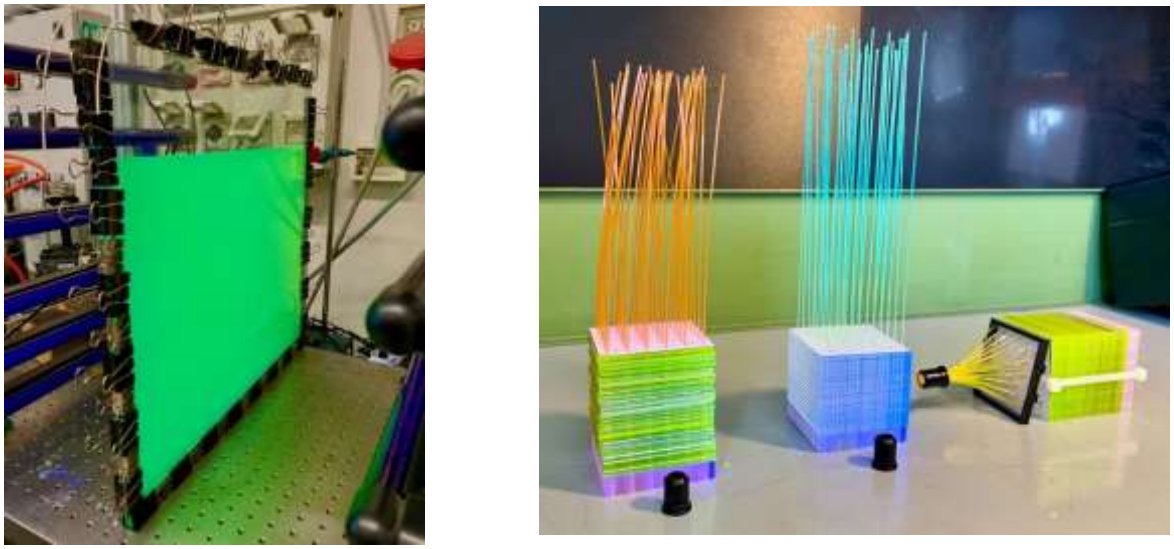

Figure 23: Left: UV polymerisation of a sheet of nanocomposite scintillator (CsPbBr3 0.2% in PMMA). Right: Shashlik assemblies tested with electron and mip beams and cosmic rays, during construction: the nanocomposite scintillator with NCA-1 WLS fibres (left), conventional scintillator (1.5% PTP + 0.04% POPOP in polystyrene) with Y-11 fibres (centre), and nanocomposite scintillator with O-2 fibres (right).

The completed prototypes were tested at CERN with 80 GeV e^- and 150 GeV π^+ beams in the SPS H2 beamline in October 2022. A second round of tests of prototypes improved based on the experience gained in October 2022 was carried out in June 2023 with 1-4 GeV e^+ and 10 GeV μ^+ beams in the PS T9. In this second round, a module constructed with the coumarin-6 wavelength-shifted $CsPb(Br,Cl)_3$ nanocomposite was also tested to evaluate this strategy for overcoming light loss from self-absorption. Unfortunately, the nanocrystals aggregated into clumps between synthesis and polymerisation of the solution, so that only limited conclusions may be drawn concerning the performance of this module.

A typical setup for the beam tests is shown in Fig. 24.

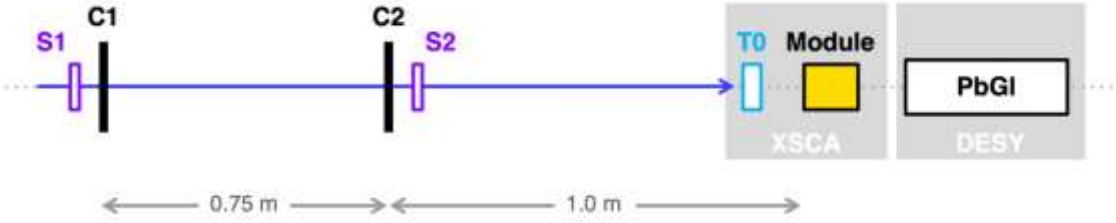

Figure 24: Setup used for the measurements of light yield in beam tests in the T9 beamline. S1 and S2 are trigger scintillators, C1 and C2 are 10x10 cm^2 silicon-strip tracking chambers with thickness 820 μm and position resolution 47 μm, T0 is a fast-timing detector, PbGl is a lead glass calorimeter for energy measurements, and the grey boxes are moveable tables.

The tracking provided by the silicon-strip chambers C1 and C2 allows the clean definition of a fiducial region for particles hitting the test module and has sufficient position and angular resolution to resolve components such as optical fibres, allowing the source of the light produced in the module to be discriminated (e.g., whether from scintillating tiles or WLS fibres). This is illustrated in Fig. 25, which shows the efficiency map obtained by illumination of the $CsPb(Br,Cl)_3$ + WLS module with 10 GeV muons and a threshold set at 5 times the RMS of the dark noise from the SiPM. Virtually all the light is produced in the optical fibres in the stack or in the bundle at the rear; very little of the light

comes from the bulk of the nanocomposite scintillator. This result is characteristic of the PMMA-based nanocomposite scintillators tested: as a rule, when exposed to single mips, the PMMA-based nanocomposites at nanocrystal concentrations of 0.2% produce at most a few percent of the light obtained from conventional scintillators. In the particular case of the $CsPb(Br,Cl)_3$ + WLS module, the poor performance may result from the problems encountered during production, so this nanocomposite formulation may still be viable and further investigation is planned. As noted in the previous section, PVT-based, thermally polymerised nanocomposites with surface-passivated CsPbBr3 nanocrystals show much more promise, and after further study and optimisation of these materials, another round of prototypes will be constructed and tested.

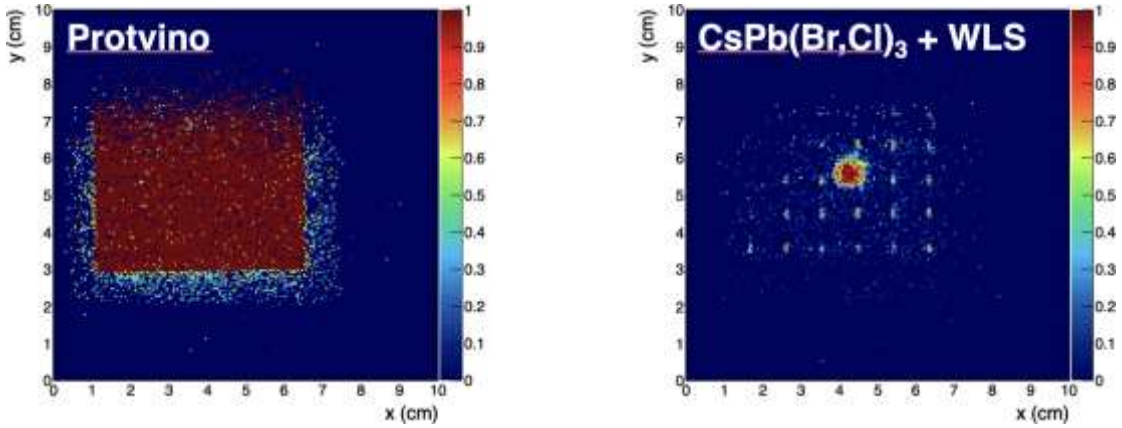

Figure 25: Response efficiency maps of shashlyk test modules illuminated with 10 GeV muons. The control module with conventional organic scintillator ("Protvino", left) shows highly efficient and uniform response to mips over the entire surface, while for the module with the nanocomposite scintillator (right), only the WLS fibres show efficient response to mips.

4. CONCLUSION

Over the last three years, several materials have been developed in Task 8.3.1 with a view to their use for detector in future high energy physics experiments. Three materials have shown promise:

- **Heavily Ce and Mg codoped GAGG scintillators with substantially accelerated decay time:**
  An optimal composition has been identified to meet the stringent requirements of the future detectors for HEP applications. The optimised scintillators are shown to be the potential candidates for the inner part of the calorimeter of the upgrade II of LHCb in 2032 [38]. First implementation of the industrial process was done in Crytur in December 2023 providing Czochralski grown crystal with diameter 25 mm and 48 mm long cylindrical part with high composition homogeneity and critical scintillation characteristics in compliance with LHCb specifications (decay time, light yield, afterglow) and within 10% difference over all the volume of the crystal.
- **The ultrafast PWO developed by Crytur:**
  The ultrafast PWO (PWO-UF) developed by Crytur was tested in several calorimeter prototypes and its excellent time resolution performance is demonstrated. The standards for the mass production of PWO scintillator is well established throughout the last three decades and evidenced to be maintained with the nearly 80000 crystals for the CMS electromagnetic calorimeter [7]. Crytur has the infrastructure and the technology in place for large scale production PWO-UF crystals. In case of high demand of PWO-UF crystals increasing the capacity of the furnaces is considered.
- **Innovative scintillator materials based on nanomaterials developed by GlasstoPower:**
  Certain properties of nanomaterials offer unique opportunities for their application in fast radiation detection in HEP experiments. Project participants developed novel fabrication techniques and demonstrated prospective properties of the novel nanoscintillators. For the first time, these innovative materials were used for high-energy physic detectors. In these last years, GlasstoPower has developed several methods to produce a large volume of nanocomposite scintillators for HEP experiments.

Several detector prototypes based on these new materials were tested in high-energy particle beams. The performance obtained allowed to provide feedback to the material producers in view to optimise the material and progress in the design of future detectors.

5. REFERENCES

[1] Auffray E et al. (2022) Test benches for testing detecting materials in picosecond and subpicosecond domains, *AIDAinnova-Milestone 32*

[2] Kamada K. et al., (2011) Composition engineering in cerium-doped $(Lu,Gd)_3(Ga,Al)_5O_{12}$ single-crystal scintillators, *Cryst. Growth Des., 10, pp4484–4490*

[3] Kamada K. et al., (2014) Cz grown 2-in. size $Ce:Gd_3(Al,Ga)_5O_{12}$ single crystal, *Optical Materials 36, pp 1942–1945.*

[4] Lucchini M. et al. *(2016),* Radiation Tolerance of LuAG:Ce and YAG:Ce Crystals Under High Levels of Gamma- and Proton-Irradiation, *IEEE Transactions on Nuclear Science 63(2), 1-1*

[5] Auffray E. et al, *(2019),* Irradiation effects on $Gd_3Al_2Ga_3O_{12}$ scintillators prospective for application in harsh irradiation environments, *Rad. Phys.Chem 164, 108365*

[6] Alenkov V. et a., (2019) Irradiation studies of a multi-doped $Gd_3Al_2Ga_3O_{12}$ scintillator, *Nucl Instrum Methods A 916, 418 pp 226-229*

[7] CMS ECAL collaboration (1997) The Electromagnetic Calorimeter Technical Design Report, CERN/LHCC 97-33

[8] Kavatsyuk, M., et al. (2011) Performance of the prototype of the electromagnetic calorimeter for PANDA, *Nucl. Instrum. Meth. A* 648, pp. 77–91.

[9] Anenkov A. et al. (2022) Lead tungstate scintillation material, *Nucl Instrum Methods A pp30-50*

[10] Nikl M. et al, Modification of $PbWO_4$ scintillator characteristics by doping, *J. Cryst. Growth **229**, 312-315 (2001)*

[11] Follin, M., et al. (2021) Scintillating properties of today available lead tungstate crystals, *J. Instrum*. 16 (8), p. P08040.

[12] Korzhik, M., et al. (2022) Ultrafast PWO scintillator for future high energy physics instrumentation, *Nucl. Instrum. Meth. A* 1034, p. 166781.

[13] Tamulaitis G, et al. (2022), Transient optical absorption as a powerful tool for engineering of lead tungstate scintillators towards faster response, *J. Materials Chemistry C, 10, 9521*

[14] Nikl M. et al. (2014) Defect Engineering in Ce-Doped Aluminum Garnet Single Crystal Scintillators, *Cryst. Growth Des. 14(9), pp 4827-4833*

[15] Nikl M., Yoshikawa A., (2015) Recent R&D Trends in Inorganic Single-Crystal Scintillator Materials for Radiation Detection**,** *Adv. Optical Mater. 2015, 3, 463–481*

[16] Kamada K. et al., (2015) Alkali earth co-doping effects on luminescence and scintillation properties of Ce doped $Gd_3Al_2Ga_3O_{12}$ scintillator**,** *Optical Materials 41 (2015) 63–66.*

[17] Lucchini M. et al., (2016) Effect of Mg^{2+} ions co-doping on timing performance and radiation tolerance of Cerium doped $Gd_3Al_2Ga_3O_{12}$ crystals, *Nucl Instrum Methods A, A816 pp:176-183.*

[18] Martinazzoli L. et al. (2021), Scintillation properties and timing performance of state-of-the-art $Gd_3Al_2Ga_3O_{12}$ single crystals, *Nucl Instrum Methods A, 1000, p165231*

[19] Talochka. Y. et al. (submitted), Acceleration of emission decay in Ce-doped Gd-containing garnets by aliovalent codoping due to blocking excitation transfer via gadolinium subsystem, *Submitted to Radiation Physics and Chemistry*

towards an ultra-accelerated scintillation response, *Mater. Adv., 3, 6842-6852*

[20] Nargelas S.et al., (2023) Influence of heavy magnesium codoping on emission decay in Ce-doped multicomponent garnet scintillators, *J. Mater. Chem C, 11, 12007-12015*

[21] Martinazzoli L. et al. (2022), Compositional engineering of multicomponent garnet scintillators:

[22] Erroi A.et al. (2023) Ultrafast and Radiation-Hard Lead Halide Perovskite Nanocomposite Scintillators, *ACS Energy Lett.* 2023, 8, 9, 3883–3894

[23] Brovelli S. et al. submitted paper.

[24] The CMS Collaboration, (2015) Technical Proposal for the Phase-II upgrade of the Compact Muon Solenoid, *CERN-LHCC-2015-010/LHCC-P-008*

[25] Benaglia A. et al. (2016), Detection of high energy muons with sub-20 ps timing resolution using L(Y)SO crystals and SiPM readout, *Nucl Instrum Methods A, 830, pp30–35.*

[26] Lucchini M. T. et al. (2017), Timing capabilities of garnet crystals for detection of high energy charged particles *Nucl Instrum Methods A, 852, pp1–19.*

[27] Cates J. et al (2018) Improved single photon time resolution for analog SiPMs with front end readout that reduces influence of electronic noise, *Phys. Med. Biol. 63*

[28] Gundacker S. et al (2019) High-frequency SiPM readout advances measured coincidence time resolution limits in TOF-PET, *Phys. Med. Biol. 64*

[29] CMS collaboration, A MIP Timing Detector for the CMS Phase-2 Upgrade, Technical Design Report, *CERN-LHCC-2019-003*

[30] Ceravolo, S., et al. (2022) Crilin: A CRystal calorImeter with Longitudinal InformatioN for a future muon collider, *J. Instrum.* 17 (9), p. P09033.

[31] Frankenthal, A. et al. (2019) Characterization and performance of PADME's Cherenkov-based small-angle calorimeter, *Nucl. Instrum. Meth. A* 919, pp. 89–97.

[32] Cemmi, A., et al. (2022) Radiation study of lead fluoride crystals, *J. Instrum. 17 (5), p. T05015*.

[33] Kozma, P., Kozma, P. Jr., and Bajgar, R. (2002) Radiation resistivity of PbF_2 crystals, Nucl. *Instrum. Meth. A* 484, pp. 149–152.

[34] Anderson, D.F., et al. (1990) Lead fluoride: An ultracompact cherenkov radiator for EM calorimetry, *Nucl. Instrum. Meth. A* 290, pp. 385–389.

[35] Auffray, E., et al. (2016) Luminescence rise time in self-activated $PbWO_4$ and Ce-doped $Gd_3Al_2Ga_3O_{12}$ scintillation crystals, *J. Lumin.* 178, pp. 54–60.

[36] Cantone, C., et al. (2023) Beam test, simulation, and performance evaluation of PbF_2 and PWO-UF crystals with SiPM readout for a semi-homogeneous calorimeter prototype with longitudinal segmentation, *Front. Phys.* 11, p. 1223183.

[37] Monti-Guarnieri, P., et al. (2022) Beam test characterization of oriented crystals in strong field conditions, In: *Proceedings of 41st International Conference on High Energy Physics* (ICHEP 2022), Bologna, Italy, 6-13 July 2022. Place of publication: *PoS* ICHEP2022, p. 342.

[38] Bandiera, L., et al. (2023) An ultra-compact and ultra-fast homogeneous electromagnetic calorimeter based on oriented lead tungstate crystals, *Front. Phys.* 11, p.1254020

[39] Gandini, M., et al. (2020) Efficient, fast, and reabsorption-free perovskite nanocrystal-based sensitized plastic scintillators, *Nat. Nanotechnol. 15, pp. 462-468.*

[40] Zhang, C., et al. (2019) Critical role of metal ions in surface engineering toward brightly luminescent and stable cesium lead bromide perovskite quantum dots, Nanoscale 11, pp. 2602-2607.

[41] Atoian, G.S., et al. (2008) An improved shashlyk calorimeter, *Nucl. Instrum. Meth A 584, pp. 291-303.*

[42] Singh, B. et al. [PANDA Collaboration] (2017) Technical Design Report for the PANDA Forward Spectrometer Calorimeter", *http://arxiv.org/abs/1704.02713v1*.

[44] LHCb collaboration (2021), Framework TDR LHCb upgrade II, *CERN/LHCC 2021-012*

ANNEX: GLOSSARY

Acronym	Definition
BaF_2	Barium Fluoride
BTF	Frascati beam test facility
Ce^{3+}	Cerium ion
CERN	Centre Europeen pour la recherche nucleaire
CL	Catholuminescence
CRILIN	Cesium lead bromide
$CsPbBr_3$	Cesium lead bromide
$CsPbCl_3$	Cesium lead chloride
EGDM	ethylene glycol dimethacrylate
EM	electromagnetic
ENEA	Italian National Agency for Energy Efficiency.
FCC	Future circular collider
GAGG	Gadolinium, gallium aluminium garnet: $Gd_3Ga_xAl_5O_{12}$
HEP	High-energy physics
HIKE	High Intensity Kaon experiment
HL-LHC	High Luminosity Large Hadron Collider
ILC	International linear collider
LARP	ligand-assisted reprecipitation
LHP	lead halide perovskite
LITG	light-induced transient gratings
LuGAGG:	Lutetium Gadolinium, gallium aluminium garnet: $(Lu,Gd)_3(Ga,Al)_5O_{12}$
LYSO, LSO	Lutetium yttrium Orthosilicate Lu_2SiO_5
Mg^{2+}	Magnesium ion
mip	Minimum ionising particle
MMA	methyl methacrylate
NC	Nano composite
PADME	Positron Annihilation into Dark Matter Experiment
PANDA	antiProton ANnihilation at Darmstadt experiment
PbF2	Lead flooride
PL	Photoluminescence
PLMA	polylaurylmethacrylate
PMMA	polymethylmethacrylate
POPOP	5-phényl-2-[4-(5-phényl-1,3-oxazol-2-yl)phényl]-1,3-oxazole

PS	polystyterne
PVT	polyvinyltoluene
PWO	Lead tungstate: $PbWO_4$
PWO-UF	Ultra fast PWO
OREO	ORiEnted calOrimeter (Compact calorimeter based on oriented crystals)
SICCAS	Shagnai institute of ceramic China academic science
STORM	STrOng cRystalline Magnetic field
RL	Radioluminescence
RMS	Root mean square
SiPM	Silicon photomultiplier
SPACAL	Sphaghetti calorimeter
SPS	Super proton synchroton
TA	Transient absorption
TRPL	time-resolved photoluminescence
UV	ultraviolet
WLS	Wavelength shifter